

# Three-dimensional surface displacements and rotations from differencing pre- and post-earthquake LiDAR point clouds

Edwin Nissen,<sup>1,2</sup> Aravindh K. Krishnan,<sup>1</sup> J. Ramón Arrowsmith,<sup>1</sup> and Srikanth Saripalli<sup>1</sup>

Received 22 May 2012; revised 29 June 2012; accepted 30 June 2012; published 16 August 2012.

[1] The recent explosion in sub-meter resolution airborne LiDAR data raises the possibility of mapping detailed changes to Earth's topography. We present a new method that determines three-dimensional (3-D) coseismic surface displacements and rotations from differencing pre- and post-earthquake airborne LiDAR point clouds using the Iterative Closest Point (ICP) algorithm. Tested on simulated earthquake displacements added to real LiDAR data along the San Andreas Fault, the method reproduces the input deformation for a grid size of ~50 m with horizontal and vertical accuracies of ~20 cm and ~4 cm, values that mimic errors in the original spot height measurements. The technique also measures rotations directly, resolving the detailed kinematics of distributed zones of faulting where block rotations are common. By capturing near-fault deformation in 3-D, the method offers new constraints on shallow fault slip and rupture zone deformation, in turn aiding research into fault zone rheology and long-term earthquake repeatability. **Citation:** Nissen, E., A. K. Krishnan, J. R. Arrowsmith, and S. Saripalli (2012), Three-dimensional surface displacements and rotations from differencing pre- and post-earthquake LiDAR point clouds, *Geophys. Res. Lett.*, 39, L16301, doi:10.1029/2012GL052460.

## 1. Introduction

[2] Large continental earthquakes produce complex patterns of ground displacements that help reveal the geometry of the causative faulting and spatial variations in fault slip. Modern satellite geodetic techniques such as radar interferometry (InSAR) and sub-pixel optical matching can map components of this deformation to high precision and over wide areas [e.g., Bürgmann *et al.*, 2000; Leprince *et al.*, 2008], but fall short of providing full three-dimensional (3-D) surface displacements. These methods are further hindered by variable coherence, with InSAR often suffering gaps in coverage close to surface faulting. This near-fault deformation is driven by shallow fault slip, the distribution of which is crucial for understanding fault zone rheology, interpreting long-term paleoseismic or geomorphic offsets, and characterizing seismic hazard.

[3] Differencing repeat airborne Light Detection and Ranging (LiDAR) datasets could potentially complement these satellite-based methods by imaging fault zone deformation in 3-D, especially in the near field (~1 km) of the rupture zone. An aircraft-mounted pulsed laser scanning system and kinematic GPS receiver are used to measure spot elevations at sub-meter intervals along saw-tooth patterned scan lines. These spot height data form irregular "point clouds", with shot densities that usually exceed ~1 points/m<sup>2</sup> and vertical and horizontal root mean square (RMS) errors that are typically 5–10 cm and 10–25 cm, respectively [e.g., Shrestha *et al.*, 1999; Toth *et al.*, 2007]. The past decade has seen an explosion in aerial LiDAR surveying along active faults in the western United States [e.g., Hudnut *et al.*, 2002; Bevis *et al.*, 2005; Prentice *et al.*, 2009], providing a baseline against which to compare future LiDAR topography collected in the aftermath of future large earthquakes along these faults. Because the sub-meter LiDAR point spacing is finer than the scale of slip in large earthquakes, 3-dimensional, near-fault ground displacements should be resolvable.

[4] The 2010 El Mayor-Cucapah (Mexico) earthquake is the only complete rupture for which pre- and post-event LiDAR data are available. A simple differencing of the gridded Digital Elevation Models (DEMs) revealed spectacular images of fault zone deformation [Oskin *et al.*, 2012], providing a tantalizing glimpse of the potential offered by differential LiDAR. However, as this approach neglects lateral motions, the resulting elevation changes do not correspond directly to surface displacements. A pair of recent studies outlined potential ways of obtaining 3-D deformation from multi-temporal LiDAR. Leprince *et al.* [2011] use image coregistration and sub-pixel correlation techniques [e.g., Leprince *et al.*, 2008] to obtain horizontal offsets from gridded LiDAR DEMs, which are then back-slipped and differenced to reveal the vertical displacements. Borsa and Minster [2012] use a set of harmonic basis functions to produce a smoothed surface through the pre-earthquake point cloud, onto which sub-sets of the post-earthquake points are translated using a least-squares minimization scheme. Both approaches include scope for incorporating LiDAR return intensities as well as elevations, but they also require gridding or smoothing of one or both datasets, an additional step which could potentially introduce biases or artifacts in the resulting displacements.

[5] In this paper, we describe a method that overcomes these problems by directly determining 3-D surface displacements from raw LiDAR point clouds using the Iterative Closest Point (ICP) algorithm [Besl and McKay, 1992; Chen and Medioni, 1992]. ICP is a technique for registering 3-D

<sup>1</sup>School of Earth and Space Exploration, Arizona State University, Tempe, Arizona, USA.

<sup>2</sup>Department of Geophysics, Colorado School of Mines, Golden, Colorado, USA.

Corresponding author: E. Nissen, School of Earth and Space Exploration, Arizona State University, Tempe, AZ 85287, USA.  
(edwin.nissen@asu.edu)

©2012. American Geophysical Union. All Rights Reserved.  
0094-8276/12/2012GL052460

images which is widely used in medicine as a way of aligning and comparing multi-temporal scans of a subject's body [e.g., Hill *et al.*, 2001] as well as in computer graphics [e.g., Levoy *et al.*, 2000]. In the Earth sciences, it has been implemented for landslide monitoring using terrestrial laser scanning datasets [Teza *et al.*, 2007], but it has not yet been

adopted for mapping tectonic deformation. Here, we summarize the ICP algorithm and outline new adaptations for its use on paired LiDAR data. Next, we simulate pre- and post-earthquake point clouds using real LiDAR data deformed with synthetic earthquakes, allowing us to explore the accuracy of the method at a range of grid sizes and input

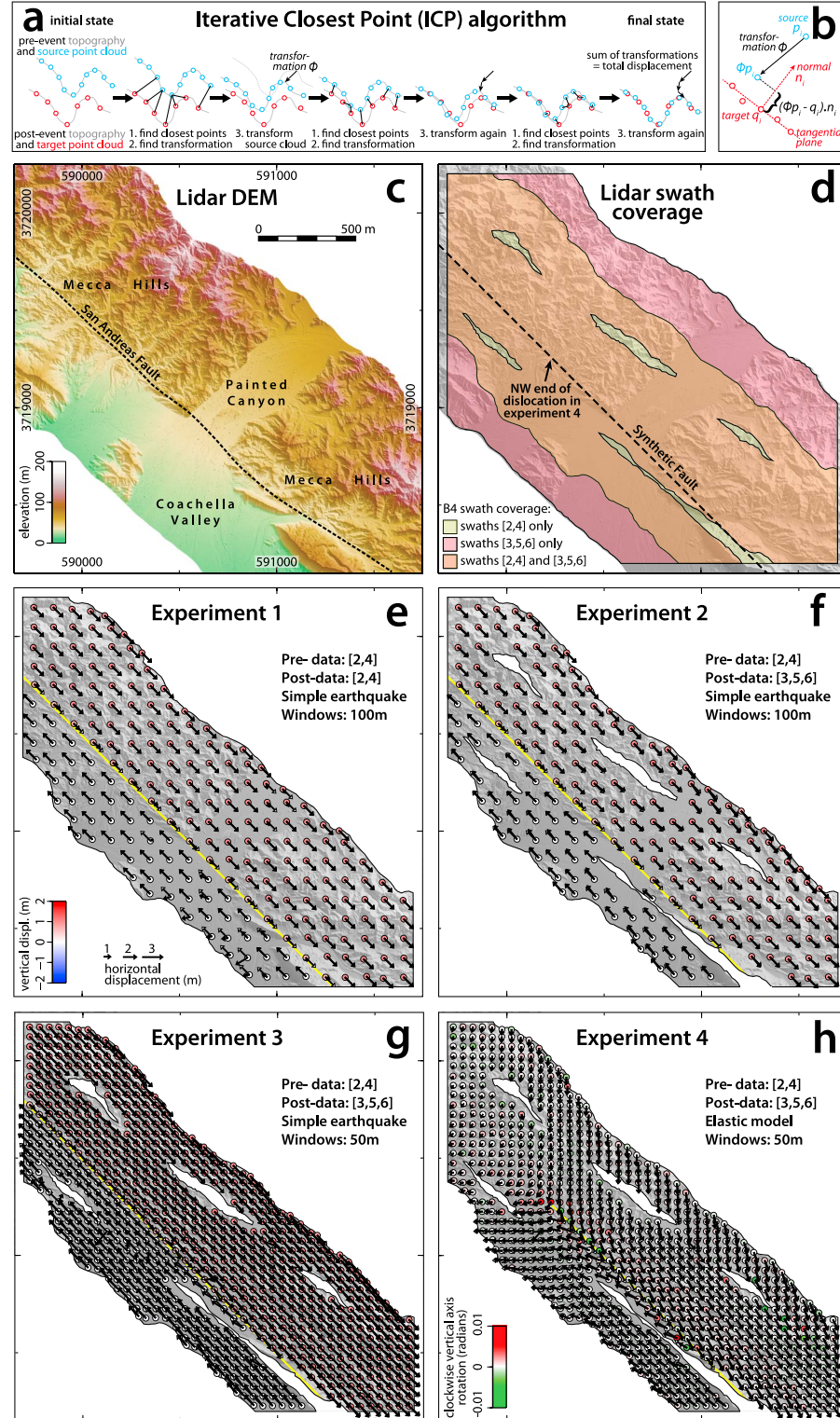


Figure 1

point cloud densities. Finally, we compare the method against alternative methods [Leprince *et al.*, 2011; Borsa and Minster, 2012] and discuss its outlook.

## 2. Method

[6] The Iterative Closest Point (ICP) algorithm aims to bring into alignment two corresponding sets of three dimensional points which sample the same object — sometimes termed the ‘source’ and ‘target’ clouds — by iterating three steps (Figure 1a). (1) For each point in the source cloud, the closest point in the target cloud is identified. (2) We compute the motion (a rigid body transformation comprising a translation and a rotation) which minimizes the mean square error (MSE) between all paired points. (3) This transformation is applied to the source cloud and the MSE is updated. These steps repeat until a local minimum in closest point distances is reached, determined when the reduction in MSE falls below some threshold.

[7] Because coseismic surface displacements will vary spatially, depending on the distance to the fault and the sense and magnitude of slip, pre- and post-event LiDAR point clouds were first split into a grid of square sub-areas, which we term ‘windows’. The ICP algorithm was then run separately on each window, with pre-event LiDAR points representing the source cloud and post-event points representing the target cloud (Figure 1a). We included target points from within a 10 m-wide margin outside the edge of the pre-event window, to ensure that features in the pre-earthquake topography were contained within the post-event window. For each window, the translations  $t_x$ ,  $t_y$  and  $t_z$  summed over all iterations correspond to the E–W, N–S and vertical coseismic displacement for that window (Figure 1a).

[8] There are several variants to the ICP algorithm which differ in the ways points are selected and matched, closest point pairs are weighted or rejected, and how the error is defined and minimized [Rusinkiewicz and Levoy, 2001]. Applied to pre- and post-earthquake airborne LiDAR point clouds, we find that the point-to-plane ICP [Chen and Medioni, 1992] yields the most accurate results. In this case, rather than defining the error as the squared sum of the distances between closest points, it is defined as the squared sum of the distances between each source point  $p_i$  and the tangential plane at its target point  $q_i$  (Figure 1b). In other words, we minimize

$$E = \sum_i \|(\phi p_i - q_i) \cdot n_i\|^2 \quad (1)$$

where  $\phi$  is the rigid body transformation and  $n_i$  is the normal to the tangent plane at  $q_i$ . Low [2004] showed that when the relative orientation of two point clouds is similar, the rotation terms can be simplified using the approximations  $\sin \theta = \theta$  and  $\cos \theta = 1$  and the non-linear optimization problem can be substituted by a linear least squares one which is easier to solve. Here,

$$\phi = \begin{pmatrix} 1 & -\gamma & \beta & t_x \\ \gamma & 1 & -\alpha & t_y \\ -\beta & \alpha & 1 & t_z \\ 0 & 0 & 0 & 1 \end{pmatrix} \quad (2)$$

where  $t_x$ ,  $t_y$  and  $t_z$  are the translation in the  $x$ ,  $y$  and  $z$  directions, and  $\alpha$ ,  $\beta$  and  $\gamma$  are the rotations in radians about the  $x$ ,  $y$  and  $z$  axes.

[9] Some aspects of our methodology, such as the subdivision of point clouds into windows and the choice of point-to-plane ICP, are similar to those used by Teza *et al.* [2007] in their study of landsliding using terrestrial LiDAR datasets. For our analysis we used the implementation of ICP in the open source Point Cloud Library [Rusu and Cousins, 2011]. In the following section we describe the experimental design and results in detail, preliminary results having been presented at a conference [Krishnan *et al.*, 2012]. The programs and experimental data we use are available for download from the website <http://robotics.asu.edu/projects/3d-registration/>.

## 3. Experimental Set-up and Results

[10] For our test area, we chose a  $\sim 2$  km-long section of the San Andreas Fault near Coachella, part of  $\sim 700$  km of the southern San Andreas and San Jacinto faults mapped in the May 2005 “B4” LiDAR survey [Bevis *et al.*, 2005]. This area encompasses parts of the jagged Mecca Hills as well as flatter alluvial deposits in Painted Canyon and the eastern Coachella Valley, allowing us to test the method for a mix of relief types over a generally sparsely-vegetated area (Figure 1c). Data were downloaded as ASCII files from the open access OpenTopography portal (<http://www.opentopography.org>). The B4 LiDAR strip is  $\sim 1.4$  km wide but actually comprises five distinct, parallel swaths, each collected on a separate flight pass and labelled 2–6 in the ASCII file (Figure 1d). Individual swaths are  $\sim 450$  m wide and contain on average  $\sim 2$  points per square meter. There are significant overlaps between adjacent swaths such that the middle  $\sim 900$  m of the overall strip is in most places covered by two swaths with a combined  $\sim 4$  points/m<sup>2</sup>. Comparisons

**Figure 1.** (a) A cross-sectional illustration of how the Iterative Closest Point (ICP) algorithm can be used to align pre- and post-earthquake topography. (b) In point-to-plane ICP, we minimize the square of  $(\phi p_i - q_i) \cdot n_i$  summed over all closest point pairs [Chen and Medioni, 1992]. The tangential plane is the best fit plane through  $k$  closest points to  $q_i$  in the target point cloud; after experimentation, we use  $k = 10$ . (c) The test area for our simulated earthquake experiments on the southern San Andreas Fault (dashed line). Topography is a 1 m-resolution DEM constructed from B4 LiDAR [Bevis *et al.*, 2005] and illuminated from the NE, and x- and y-axes show UTM zone 11 coordinates in meters. (d) B4 LiDAR coverage separated by flight number, with swaths 2 and 4 in yellow, swaths 3, 5 and 6 in pink, and areas covered by both sets of swaths in orange. The synthetic fault used in our experiments is plotted as a dashed line. (e) Results of our first ICP analysis on synthetic earthquake data: white and black arrows show input and output horizontal displacements, respectively, and coloured circles show output vertical displacements. The synthetic fault is plotted in yellow. (f) Results of our second experiment, in which pre- and post-event point clouds are taken from separate LiDAR swaths. (g) Results for a reduced window size of 50 m. (h) Results for the elastic dislocation model described in the text for a window size of 50 m. In this panel coloured circles represent vertical axis rotations (clockwise in red and anticlockwise in green).

with ground control points suggest that mean horizontal errors are  $\sim 25$  cm and mean vertical errors are  $\sim 6$  cm [Toth *et al.*, 2007], although atmospheric path delays in the kinematic GPS positioning of the aircraft may have caused an additional vertical uncertainty of  $\sim 15$  cm [Shan *et al.*, 2007].

[11] For our first experiment, we combined data from swaths 2 and 4, which cover the middle  $\sim 900$  m of the B4 strip and contain in total  $\sim 4.3$  million points (Figure 1d). The unfiltered point cloud was used as a pre-event dataset, and we deformed these exact same points using a simple, simulated right-lateral earthquake to form a post-event dataset. The planar and vertical synthetic fault strikes NW through the center of the dataset, close to the real surface trace of the SAF (Figure 1d); all post-event points NE of the fault were shifted 2 m towards the SE, and points SW of the fault were moved 2 m towards the NW. In order to test vertical displacement detection, we also raised points on the NE of the fault by 1 m. The total slip magnitude is similar to that expected for a shallow continental earthquake of  $M_w$  7–7.5. This approach is similar to that of *Borsa and Minster* [2012], though their test area was smaller ( $\sim 800$  m  $\times$  400 m) and flatter, containing little variation in landscape type.

[12] Results for an initial square window size of  $100 \times 100$  m are displayed in Figure 1e. Displacements are plotted at the weighted center of each point cloud window, with white arrows showing the input horizontal motions, black arrows showing retrieved horizontal motions, and coloured circles showing retrieved uplift or subsidence. Retrieved rotations are negligible, as expected, and so these are not plotted. Windows containing the fault encompass points moving in opposite directions, and correspondingly show small overall motions. Away from the fault, input displacements are reproduced very well, with  $>90\%$  of window results agreeing with the input displacements to better than 1 cm in all three (E-, N- and vertical) components. However, small patches of flat-lying ground in the Coachella Valley and Painted Canyon show anomalous displacements, highlighting the fact that low-relief areas probably contain several local minima in the error function, with ICP not always converging on the correct one.

[13] This first experiment is not a realistic test of differential LiDAR techniques, because the exact same points — collected from the same flight passes and along the same scan lines — were used as the basis for both pre- and post-event datasets. In reality, pre- and post-earthquake datasets will have been captured on separate flights with different scan line patterns and point distributions on the ground. For a more realistic test of our method, we therefore conducted a second experiment in which we differentiated pre- and post-earthquake points by splitting the original data according to flight pass number. Swaths 2 and 4 still form the pre-event topography, but swaths 3, 5 and 6 were used as the basis for the post-event data and deformed in the same way as in the first experiment. Pre- and post-event datasets both have average point cloud densities of  $\sim 2$  points/m $^2$ , with a few small areas containing double this amount ( $\sim 4$  points/m $^2$ ). The post-event dataset also contains a few thin gaps (shown in yellow in Figure 1d) where outer swaths 5 or 6 do not fully overlap the central swath 3. In total, there are  $\sim 4$  million points within the overlapping parts of each dataset.

[14] Displacement results for a window size of  $100 \times 100$  m are shown in map view in Figure 1f and in histogram

form in the top line of Figure 2. At this grid size, ICP analysis took  $\sim 1$  hour to run on a standard desktop computer (Figure 2). As before, windows encompassing the fault have small overall displacements; in addition, those which include patches with no post-event points produce anomalous results, which we removed. Elsewhere, there is a good match between input and output horizontal and vertical displacements, even in flat-lying areas. Root mean square (RMS) errors are  $\sim 13$  cm and  $\sim 15$  cm for E- and N-displacements,  $\sim 4$  cm for vertical displacements, and  $\sim 5^\circ$  for displacement azimuths, values that mimic estimated errors in the original B4 data [Toth *et al.*, 2007]. In some areas, small mismatches are spatially correlated; these errors reverse in sense when the swaths used for pre- and post-event data are switched, hinting that they are caused by geo-referencing discrepancies between different flight lines in the original dataset [Shan *et al.*, 2007].

[15] We repeated the analysis using progressively smaller window dimensions of 50 m (Figure 1g), 25 m and 15 m. As the window size is reduced, processing times increase and accuracies diminish (Figure 2). RMS errors in E-W and N-S displacements are 21–22 cm for 50 m windows and 30–39 cm for 25 m windows, while vertical errors remain  $\sim 4$  cm for 50 m windows but increase to  $\sim 16$  cm for 25 m windows. At 15 m resolution, we find that the method breaks down altogether and is unable to reproduce input displacements. This may reflect a threshold of around 500–1000 in the number of points required for ICP to yield accurate results with these data.

[16] We also repeated these experiments using pre- and post-event point clouds with sparser densities, created by removing data on a point by point basis from the original cloud. With both datasets reduced to  $\sim 0.25$  points/m $^2$  (one eighth of the original density), and with window dimensions of  $100 \times 100$  m, RMS errors increase to  $\sim 40$  cm for E- and N-displacements,  $\sim 12$  cm for vertical displacements, and  $\sim 16^\circ$  for azimuth. Similar errors were obtained when only the pre-event point cloud density was reduced. This implies that the accuracy of our method depends on sparser of the two datasets, but it also shows that ICP works well even with large mismatches in point cloud density — an important consideration given that modern LiDAR point cloud densities may exceed those of older datasets by several orders of magnitude [e.g., *Osokin et al.*, 2012]. These results also suggest that in the future, when LiDAR surveys may exceed 10 points/m $^2$  as standard, ICP could resolve displacements at grid sizes much finer than 25 m.

[17] Observed earthquake surface displacements are much more heterogeneous than those in our initial, simple model. Point cloud windows are likely to accommodate small amounts of internal strain and some windows may also rotate. As a fourth and final experiment, we investigate whether ICP can detect more realistic, spatially heterogeneous displacements, using a dislocation in an elastic half-space [Okada, 1985] to simulate the complex pattern of deformation expected at the end of a strike-slip rupture. Our synthetic rupture again strikes NW, but its north-western end lies in the center of the dataset (Figure 1d). To form the post-earthquake dataset, we place 4 m of right-lateral slip along this fault, compute the resulting x, y and z surface displacements at each point in swaths 3, 5 and 6 and add these displacement to the point co-ordinates. Results for a window size of  $50 \times 50$  m are shown in Figure 1h. The smooth

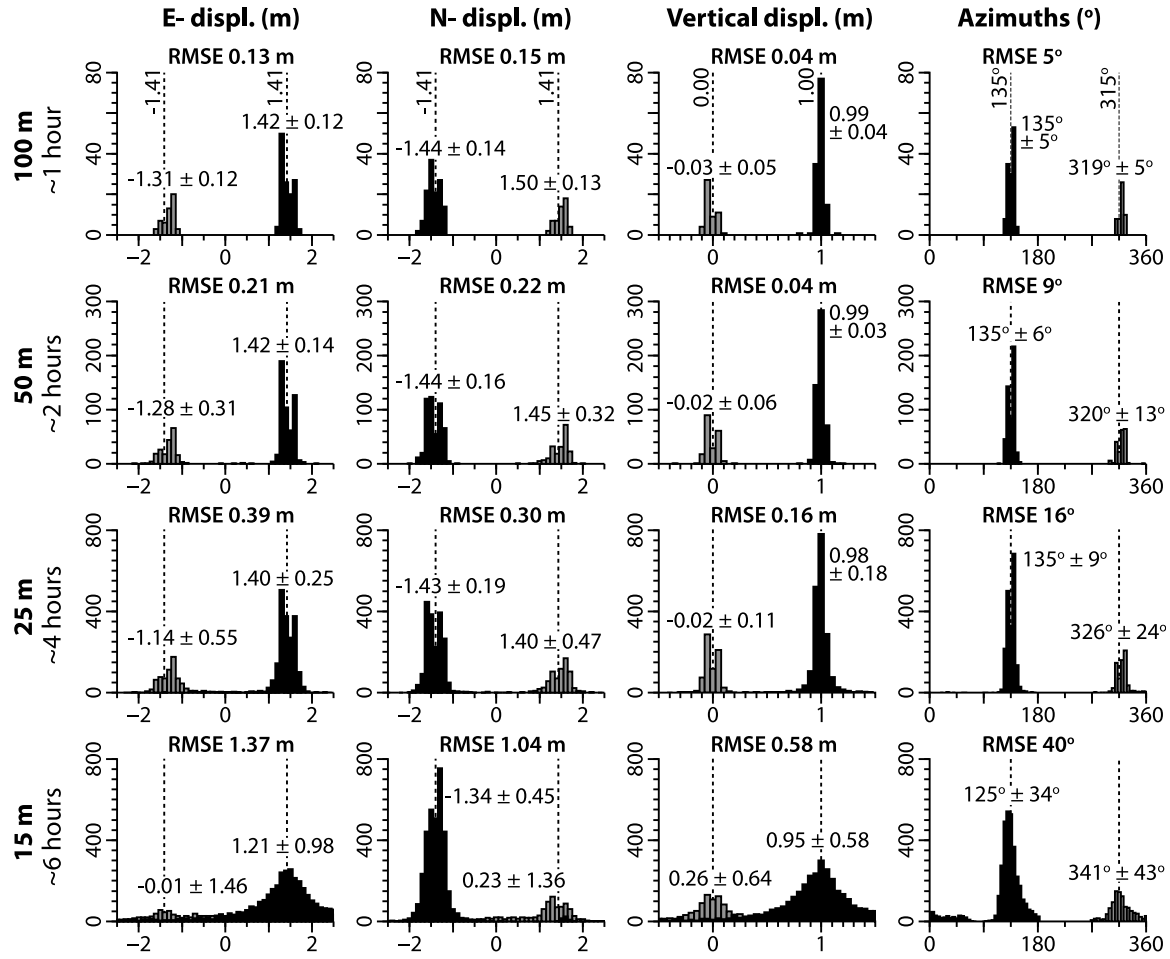


**Figure 2.** Histograms of ICP results for the synthetic earthquake in Experiment 2, for a variety of window sizes. From top to bottom, these show results for window dimensions of 100 m, 50 m, 25 m and 15 m; processing times are plotted next to the window size (we used a Quad Core Intel 2.6 GHz processor with 4 GB of RAM). From left to right, they show E–W displacements and N–S displacements (both with bin widths of 0.1 m), vertical displacements (bin widths of 0.05 m), and displacement azimuths (bin widths of 5°). Histogram y-axes show number of windows within each bin, with black bars representing windows NE of the fault and grey bars showing those SW of the fault; windows containing the fault itself are excluded. Overall root mean square errors (RMSE) are shown above each histogram, with mean values and 1  $\sigma$  uncertainties plotted separately for results on either side of the fault. The expected (input) values are marked by vertical dashed lines.

pattern of strain at the end of the fault is reproduced well, with overall RMS errors of  $\sim 17$  cm,  $\sim 18$  cm and  $\sim 4$  cm for E-, N- and vertical displacements. The results also include direct measurements of small clockwise rotations ( $<0.01$  radians) at the NW end of the dislocation which are shown as coloured circles in Figure 1h.

#### 4. Discussion and Conclusions

[18] We have described an adaptation of the ICP algorithm that calculates 3-D coseismic surface displacements from pre- and post-earthquake LiDAR topography. The method works at acceptable speeds even on a standard desktop computer, and can recover complex patterns of deformation at grid sizes of  $\sim 25\text{--}50$  m for point cloud datasets with  $\sim 2$  points/m<sup>2</sup>. For 50 m window dimensions, horizontal and vertical errors are  $\sim 20$  cm and  $\sim 4$  cm respectively, values that mimic and are probably related to errors in the raw LiDAR spot elevations. Accuracies are

highest in windows containing rugged topography but the method is mostly successful even in low-relief areas. Our analysis does not take into account the potential effects of ground shaking, erosion and deposition, vegetation growth or infrastructure development, but as long as these processes occur on shorter length-scales than the ICP grid size they are unlikely to impact the results. While we concentrate on its application to faulting, ICP could potentially be applied to other displacing processes such as glaciers or deep-seated landsliding [e.g., Teza *et al.*, 2007].

[19] Although alternative methods achieve somewhat finer resolutions — Leprince *et al.* [2011] and Borsa and Minster [2012] cite pixel dimensions of  $\sim 5$  m and  $\sim 15$  m, respectively — our method utilizes only the original point clouds and is thus free from artifacts or biases that might arise from representing the topography with a smoothed surface model or gridded DEM. ICP is well suited to handling very large datasets and works well even when there are large mismatches in the density of the two point clouds, eliminating

the need to downsample the denser dataset. A final, unique aspect of our method is that it can measure rotations directly, thus providing important new kinematic data in areas of distributed faulting where block rotations may be important. In the future, ICP should be able to obtain smaller grid sizes and improved precisions using higher point cloud densities and with further advances in survey geo-referencing. We also note the potential for incorporating LiDAR intensity data — using ICP, sub-pixel correlation or particle image velocimetry [Aryal *et al.*, 2012] — as an additional, independent constraint on horizontal displacements in flat regions.

[20] Applied to future earthquakes spanned by repeat LiDAR datasets, ICP will provide a wealth of near-fault displacement data to complement existing geodetic or field-based observations. These displacements will help constrain the slip distribution and rheology of the shallow part of the fault zone, which are crucial for interpreting paleoseismic and geomorphic offsets and will inform studies of long-term earthquake behavior. When coupled with satellite-based measurements such as InSAR, differential LiDAR will also offer the means to explore relations between surface rupturing and deeper fault zone processes. Finally, the development of this method provides further impetus to efforts at expanding the range of active faults mapped with LiDAR.

[21] **Acknowledgments.** Our research was supported through the Southern California Earthquake Center, a grant from the National Science Foundation (EAR-1148302), and a SESE Exploration Fellowship to E. N. We thank all those involved in the B4 project, including Ohio State University, the US Geological Survey, the National Center for Airborne Laser Mapping (NCALM), UNAVCO, the Southern California Integrated GPS Network (SCIGN) and Optech International. The project was funded by the EAR Geophysics program at the National Science Foundation (NSF) and relied on the generosity of many landowners along the fault zones. LiDAR data were provided by the OpenTopography Facility with support from the National Science Foundation under NSF awards 0930731 and 0930643. We thank Adrian Borsa, Alejandro Hinojosa Corona, Ken Hudnut, Sébastien Leprince and Michael Oskin for many discussions on this exciting new topic of research, as well as two anonymous reviewers for helping improve the paper.

## References

- Aryal, A., B. A. Brooks, M. E. Reid, G. W. Bawden, and G. R. Pawlak (2012), Displacement fields from point cloud data: Application of particle imaging velocimetry to landslide geodesy, *J. Geophys. Res.*, **117**, F01029, doi:10.1029/2011JF002161.
- Besl, P. J., and N. D. McKay (1992), A method for registration of 3-D shapes, *IEEE Trans. Pattern Anal. Mach. Intell.*, **14**, 239–256, doi:10.1109/34.121791.
- Bevis, M., et al. (2005), The B4 Project: Scanning the San Andreas and San Jacinto Fault Zones, *Eos Trans. AGU*, **86**(52), Fall Meet. Suppl., Abstract H34B-01.
- Borsa, A., and J. B. Minster (2012), Rapid determination of near-fault earthquake deformation using differential lidar, *Bull. Seismol. Soc. Am.*, in press.
- Bürgmann, R., P. A. Rosen, and E. J. Fielding (2000), Synthetic Aperture Radar interferometry to measure the Earth's surface topography and its deformation, *Annu. Rev. Earth. Planet. Sci.*, **28**, 169–209.
- Chen, Y., and G. Medioni (1992), Object modelling by registration of multiple range images, *Image Vision Comput.*, **10**(3), 145–155.
- Hill, D. L. G., P. G. Batchelor, M. Holden, and D. J. Hawkes (2001), Medical image registration, *Phys. Med. Biol.*, **46**(3), R1–R45.
- Hudnut, K. W., A. Borsa, C. Glennie, and J.-B. Minster (2002), High-resolution topography along surface rupture of the 16 October 1999 Hector Mine, California, earthquake (Mw 7.1) from Airborne Laser Swath Mapping, *Bull. Seismol. Soc. Am.*, **92**, 1570–1576, doi:10.1785/0120000934.
- Krishnan, A. K., E. Nissen, S. Saripalli, R. Arrowsmith, and A. H. Corona (2012), Change detection using airborne lidar: Application to earthquakes, in *International Symposium on Experimental Robotics*, pp. 1–11, Springer, Berlin.
- Leprince, S., E. Berthier, F. Ayoub, C. Delacourt, and J.-P. Avouac (2008), Monitoring Earth surface dynamics with optical imagery, *Eos Trans. AGU*, **89**(1), 1, doi:10.1029/2008EO010001.
- Leprince, S., K. W. Hudnut, S. O. Akciz, A. Hinojosa-Corona, and J. M. Fletcher (2011), Surface rupture and slip variation induced by the 2010 El Mayor-Cucapah earthquake, Baja California, quantified using COSI-Corr analysis on pre- and post-earthquake LiDAR acquisitions, Abstract EP41A-0596 presented at 2011 Fall Meeting, AGU, San Francisco, Calif., 5–9 Dec.
- Levoy, M., et al. (2000), The Digital Michelangelo Project: 3D scanning of large statues, in *Computer Graphics: SIGGRAPH 2000 Conference Proceedings*, pp. 131–144, ACM Press, New York.
- Low, K. L. (2004), Linear least squares optimization for point-to-plane ICP surface registration, *Tech. Rep. TR04-004*, Dep. of Comput. Sci., Univ. of N. C. at Chapel Hill, Chapel Hill.
- Okada, Y. (1985), Surface deformation due to shear and tensile faults in a half-space, *Bull. Seismol. Soc. Am.*, **75**, 1135–1154.
- Oskin, M. E., et al. (2012), Near-field deformation from the El Mayor-Cucapah earthquake revealed by differential LiDAR, *Science*, **335**, 702–705, doi:10.1126/science.1213778.
- Prentice, C. S., C. J. Crosby, C. S. Whitehill, J. R. Arrowsmith, K. P. Furlong, and D. A. Phillips (2009), Illuminating Northern California's active faults, *Eos Trans. AGU*, **90**(7), 55, doi:10.1029/2009EO070002.
- Rusinkiewicz, S., and M. Levoy (2001), Efficient variants of the ICP algorithm, in *Proceedings of the Third International Conference On 3-D Digital Imaging and Modeling*, pp. 141–152, IEEE Comput. Soc., Los Alamitos, Calif.
- Rusu, R. B., and S. Cousins (2011), 3D is here: Point Cloud Library (PCL), in *IEEE International Conference on Robotics and Automation (ICRA)*, pp. 1–4, Inst. of Electr. and Electron. Eng., Shanghai, China.
- Shan, S., M. Bevis, E. Kendrick, G. L. Mader, D. Raleigh, K. Hudnut, M. Sartori, and D. Phillips (2007), Kinematic GPS solutions for aircraft trajectories: Identifying and minimizing systematic height errors associated with atmospheric propagation delays, *Geophys. Res. Lett.*, **34**, L23S07, doi:10.1029/2007GL030889.
- Shrestha, R. L., W. E. Carter, M. Lee, P. Finer, and M. Sartori (1999), Airborne Laser Swath Mapping: Accuracy assessment for surveying and mapping applications, *J. Am. Congr. Surv. Mapp.*, **59**(2), 83–94.
- Teza, G., A. Galgaro, N. Zaltron, and R. Genevois (2007), Terrestrial laser scanner to detect landslide displacement fields: A new approach, *Int. J. Remote Sens.*, **28**(16), 3425–3446.
- Toth, C., D. Brzezinska, N. Csanyi, E. Paska, and N. Yastikli (2007), LiDAR mapping supporting earthquake research of the San Andreas fault, in *Proceedings of the ASPRS 2007 Annual Conference*, pp. 1–11, Am. Soc. for Photogramm. and Remote Sens., Bethesda, Md.